Transitional subphases near the electric-field-induced phase transition to the ferroelectric phase in Se-containing chiral smectic liquid crystals observed by resonant x-ray scattering

Atsuo Iida, Yoichi Takanishi, Atsuo Fukuda, and Jagdish K. Vij

Phys. Rev. E **94**, 052703 — Published 14 November 2016

DOI: 10.1103/PhysRevE.94.052703

Transitional subphases near the electric field-induced phase transition to the ferroelectric phase in Se-containing chiral smectic liquid crystals observed by resonant X-ray scattering

Atsuo Iida[1)], Yoichi Takanishi[2)], Atsuo Fukuda[3)] and Jagdish K. Vij[3)]

1) Photon Factory, Institute of Materials Structure Science, High Energy Accelerator Research Organization, 1-1 Oho Tsukuba, Ibaraki 305-0801, Japan
2) Department of Physics, Faculty of Science, Kyoto University, Kitashirakawa-oiwake, Sakyou-ku Kyoto 606-8502, Japan
3) Department of Electronic and Electrical Engineering, Trinity College, The University of Dublin, Dublin 2, Ireland

Abstract

Resonant X-ray scattering experiments revealed new transitional subphases near the electric field-induced phase transition of a Se-containing chiral liquid crystal in a planar aligned cell geometry. In the lower temperature range (SmC_A^* and 3-layer periodicity SmC_γ^* phases), the 6-layer periodicity subphase appeared with increasing electric field during the field-induced transition from SmC_γ^* to SmC^*. In the higher temperature range (4-layer periodicity AF phase), the peak positions of the 3-layer satellites shifted to those of the 4-layer satellites and then the satellites corresponding to the 5- through 7-layer periodicity appeared in sequence. Near the AF to SmC_α^* phase transition temperature, the layer periodicity increased with applied field. The molecular configurations of the subphases near the field-induced transition are discussed based on the Ising, distorted clock, and perfect clock models.

I. Introduction

Ferroelectric, antiferroelectric, and ferrielectric phases are realized in certain chiral smectic (tilted) C liquid crystals (LCs). These phases are characterized by the one-dimensional layer structure and by the tilted director (the molecular average direction) change from layer to layer [1, 2]. With decreasing temperature, the phases usually appear in the order of ferroelectric SmC^*, antiferroelectric AF (SmC^*_{FI2}, SmC^*_{d4}, or $SmC^*_A(q_T = 1/2)$), ferrielectric SmC^*_γ (SmC^*_{FI1}, SmC^*_{d3}, or $SmC^*_A(q_T = 1/3)$), and antiferroelectric SmC^*_A [2-9]. Resonant X-ray scattering (RXS) directly determined the SmC^*_γ and AF layer structures as 3-layer and 4-layer periodicity phases, respectively [10-14]. Furthermore, the tilted SmC^*_α phase, appearing below the SmA phases, was assigned to a phase with an incommensurate short pitch [10, 15, 16]. The origin of the long-range interlayer interactions expected in these phases has been discussed theoretically [17-21]. Recently, a new smectic phase with an antiferroelectric 6-layer periodicity was found between the SmC^* and SmC^*_α phases by Wang *et al.* using RXS [22-24]. Takanishi *et al*. also observed a 6-layer periodicity phase between the SmC^* and SmC^*_A phases in the mixture with Br-containing LCs [25] and a 10-layer periodic structure in the B2 phase of a bent core LC doped with chiral molecules [26].

In an electric field, these LCs undergo an electric field-induced phase transition from the antiferroelectric and ferrielectric phases in a low applied field to the SmC^* phase in a high field. Extensive studies of the field-induced phase transitions were performed using the optical, electric

and other techniques [3, 6, 27-32]. Recent RXS studies under an electric field directly revealed the electric field-induced phase transitions from the low field AF phase to the high field SmC_{γ}^{*} phases [33-35]. In these experiments, the planer aligned cell structure (device geometry) was adopted to apply a sufficiently high electric field, while most of the RXS experiments were performed using self-standing films [10-15, 22].

We have reported a new field-induced transitional subphase with a very long period of 12 layers between the SmC_{γ}^{*} phase and the SmC^{*} phase in a Br-containing chiral LC by combining X-ray microbeam RXS with the cell structure [36]. The theoretical studies of the intermediate phases in the presence of an electric field suggested the induction of the ferrielectric phase [37] and the stabilization of the 12-layer and 15-layer periodicity subphase [38]. Investigating the transitional subphases and their molecular arrangements in other LC materials under the electric field can clarify the underlying mechanisms of the phase transition process. In this paper, the electric field-induced phase transitions at several temperatures are studied using the RXS technique for the Se-containing chiral smectic LC, which is a typical LC for RXS measurements [11, 13, 32, 34, 35]. We observe new field-induced transitional subphases and the successive change of the layer periodicity. The molecular configurations of the subphases near the field-induced transition are discussed from the RXS point of view.

II. Experimental

A Se-containing LC sample (AS657) [11, 32, 36, 37], purchased from Kingston Chemicals Ltd, University of Hull, Hull, U.K. (Fig.1), was used in the experiments, which had the phase sequence of SmC_A^* (82.0 °C) SmC_γ^* (83.5 °C) AF (85.9 °C) SmC_α^* → SmA → Iso with heating. The phase transition temperatures were obtained during the X-ray experiments.

The details of the experimental conditions were provided elsewhere [41], and the brief summary is presented here for convenience. The sample was sandwiched between two 80 μm-thick glass plates coated with indium tin oxide as electrodes. The cell thickness was about 25 μm. One side of the glass plate was coated with polyimide and rubbed. To obtain a uniform layer structure, a square-wave electric field (±98 V maximum) was applied around 80 °C, and then the sample was heated to the target phase. The sample cell was mounted on a compact heater, which had small windows (2 mm in diameter) for X-ray transmission. A platinum resistance thermometer sensor measured the temperature very close to this window. The samples were examined from 81 °C (SmC_A^*) to 86 °C (SmC_α^*). The applied alternating electric field was a square waveform of 100 Hz. Measurements were always performed with increasing electric field.

RXS experiments were performed on the 4A beamline at the Photon Factory (Japan). A monochromatic X-ray microprobe with a 5-μm^2 beam size was used. The layer normal was approximately horizontal and a vertical rotation axis was adopted. The incident X-ray energy was

set to the absorption edge of Se (12.65 keV). A pixel array X-ray detector (Pilatus-100K, DECTRIS) was located 85 cm through 100 cm from the sample. The exposure time ranged from 10 min to 30 min, depending on the experimental conditions. A polarizing optical microscope monitored the optical response of the sample during the measurement. The phase boundaries were usually clearly observed due in part to the spatial temperature gradient in the sample (about 0.2 °C/200 μm). The sample temperature stability was better than ±0.03 °C during the measurement. The measurement was always carried out with increasing temperature and the temperature calibration between different samples and several experimental runs was performed by measuring the major phase transition temperature with the help of optical microscope observation.

RXS satellite reflections from the subphase at the resonant condition appear at $q/q_0 = l + m((1/\nu) \pm \varepsilon)$, where q is the scattering vector, $q_0 = 2\pi/d$ (d is the smectic layer spacing), l and m (±1, ±2, ±3..) are integers, ν is the number of layers in a unit cell, $\varepsilon = 1/p$, and p is the optical pitch in units of d [10, 42]. At each applied electric field, the first order X-ray diffraction intensity was measured as a function of the sample rotation angle (the ω-angular intensity profile) to characterize the local layer structure and to determine the Bragg condition. Then, the incident angle was adjusted to the satellite peak position of interest. The q/q_0 intensity distribution in the radial direction was extracted from the recorded two-dimensional (2D) pattern. The first order Bragg peak position in the 2D pattern was approximated as q_0 and the obtained intensity distribution was

analyzed semi-quantitatively. The intensity distribution from the cell structure sample was sensitive to the stability and perfection of the layer structure that was deduced from the ω-angular intensity profiles, i.e. various types of the chevron structures [43]. Furthermore, the changes of the layer Bragg peak position and its profile during the measurement at a specific temperature were not detected, therefore, together with analysis of the the ω-angular intensity profile, the effect of the strain was not critical in the present experiment. The RXS reflections appearing near the forward scattering direction ($q/q_0 < 1$) were measured to attain reasonable detection efficiency, while a direct beam stopper blocked scattered X-rays in the small q region. From geometrical conditions, the practical q/q_0 resolution of the measurement was less than 0.005, though it depended on the counting statistics in practice. Finally, the RXS intensity in the present experiment was mainly due to $\sigma\pi$ scattering (π incident and σ scattered X-rays) because the incident beam was π polarized with respect to the reflection plane in our experimental arrangement and that the RXS theory predicts that the contribution from $\pi\pi$ scattering is very weak [40].

III. Experimental results

A. Below 83.5 °C (SmC_A^* and SmC_γ^* phases)

At 81.6 °C, the sample was in the antiferroelectric phase (SmC_A^*). An optical micrograph showed the homogeneous structure (Fig. 1 (a)), and no appreciable optical response to the applied electric field was observed in an applied field below ±30 V. The ω-angular distribution contained a double peak, which indicated a vertical chevron layer structure (Fig. 1 (e)). The two 1/2-order RXS satellite reflections appeared due to the 2-layer periodicity (C_{2p} hereafter) with a long period helical structure (Fig. 2 (a)), which was obtained at an incident angle adjusted to $q/q_0 = 1/2$ with respect to the lower angle peak of the ω-angular distribution in Fig. 1 (e).

At an applied field of ±30 V, a new phase with a thick stripe-like pattern running parallel to the boundary appeared from the left side of the view field and gradually moved to the right (Fig. 1 (b)). The RXS pattern changed with time because of this boundary movement. The first measurement showed the *m*/3- and 1/2-order reflections (broken line in Fig. 2 (b)) and the second measurement at the same conditions revealed the *m*/3-order reflections alone (solid line in Fig. 2 (b)). At a slightly higher voltage (±31 V), there were no 1/2-order reflections (Fig. 2 (c)). The field-induced phase transition from the C_{2p} phase to the 3-layer periodic structure (C_{3p} hereafter) occurred at this voltage without an intermediate state.

The C_{3p} phase was stable up to ±80 V, while the stripe-like texture vanished around ±40 V and

a crease-like texture appeared around ±60 V. The vertical chevron structure gradually changed to a compound chevron structure (combination of horizontal and vertical chevrons) and then transformed to the bookshelf structure above ±40 V (Fig. 1 (f)). At ±80.3 V (solid line in Fig. 2 (d)), the intensity of the *m*/3-order reflections decreased and the reflections at q/q_0 = 3/6 and 5/6 appeared. These peak positions corresponded to the *m*/6-order reflections of the 6-layer periodicity (C_{6p}), though the reflection at q/q_0 = 1/6 was not observed due to the direct beam stopper. The peak widths of these reflections were several times broader than the *m*/3-order reflections in the C_{3p} phase. At ±80.4 V, the peak positions shifted slightly from the original positions with a split of the 3/6 reflection (Fig. 2 (e)). At ±81 V, the lowest order peaks were around q/q_0 = 0.31 and the other peaks became broader and weaker. The diffraction intensity at ±82.0 V (Fig.2 (g)) contained a broad peak around q/q_0 = 0.28 and a very weak and broad intensity increase around q/q_0 = 0.4, 0.6, and 0.72, which seemed to be related to the C_{7p} configuration (*m*/7-order reflections). However, in this case, the diffraction profile obtained from the adjacent position (20 μm apart) showed the clear 6/7-order peak. There were no clear peaks around ±85.1 V, but the background remained (solid line in Fig. 2 (h)) and the 2D diffraction pattern showed a "streak" (inset A in Fig. 2 (h)). The optical micrograph showed a new weak boundary between the C_{7p}-like subphase and the streak subphase (Fig. 1 (c)). At a higher voltage, the phase transition to the SmC^* phase occurred (Fig. 1 (d)) and the streak vanished (dotted line in Fig. 2 (h) and inset B).

At 82.2 °C (0.2 °C above the SmC_A^* to SmC_γ^* phase transition temperature), the RXS showed the C_{3p} phase below ±71.0 V (Fig. 3 (a)). Although the layer structure changed from the vertical chevron structure to the bookshelf structure around ±20 V, no remarkable texture changes were observed during the C_{3p} phase. The *m*/3-order reflections became weaker at ±71.0 V, and the weak humps at q/q_0 = 3/6 and 5/6 seemed to appear (C_{6p}. Fig. 3 (b)). At ±71.1 V, broad peaks appeared at q/q_0 = 0.32, 0.68, and 0.84 together with a broad weak hump around q/q_0 = 3/6 (Fig. 3 (c)). At a higher voltage, the lowest order peak shifted to a smaller *q* value and the other peak intensities became very weak (Fig. 3 (d)); then the streak background appeared (solid line in Fig. 3 (e)). Some of the broad peak positions in Fig. 3 (d) (q/q_0 = 2/7 and 5/7) might relate to the C_{7p} structure. Around ±71 V (C_{3p} to C_{6p} transition) and ±75 V ("streak" to SmC* phase transition), the boundary with a weak contrast that ran parallel to the layer moved across the field of view.

Furthermore, at 83.0 °C (0.5 °C below the SmC_γ^* to AF phase transition temperature), the applied field dependences of the RXS profiles were quite similar to those at 82.2 °C, except the field-induced phase transition started at ±50 V and changed to the SmC^* phase at ±59 V. In summary, the applied field dependencies of the RXS profiles near the phase transition from SmC_γ^* to SmC^* at 81.6 °C, 82.2 °C and 83.0 °C were similar to each other.

B. Above 83.5 °C (AF and SmC_α^* phases)

At 83.9 °C (0.4 °C above the SmC_γ^* to AF phase transition temperature), the RXS pattern showed the reflections at q/q_o = 1/4 and 3/4 up to ±19 V (Fig. 4 (a)), which indicates the antiferroelectric 4-layer periodicity phase (C_{4p1}). The polarizing microscope image showed the weak stripe texture running parallel to the smectic layer. At ±19 V, the stripe texture gradually disappeared and the C_{4p1} phase changed to the C_{3p} phase, as shown in Fig. 4 (b). The C_{3p} phase was stable up to ±28 V. Then, the *m*/3-order peaks gradually shifted to the *m*/4-order peaks up to ±36 V (Fig. 4 (c), (d), and (e)). At ±31 V, extra subpeaks appeared around q/q_o = 0.42 and 0.58. Weak and broad stripes were seen in the field of view above ±36 V (similar to Fig. 1(c)). With increasing voltage, the C_{5p} subphase at ±38 V (Fig. 4 (f)), the C_{6p} subphase at ±40 V (Fig. 4 (g)), and the C_{7p} subphase at ±42 V (Fig. 4 (h)) appeared in sequence; however, the $1/\nu$ reflections (ν = 5 to 7) were barely seen or not observed due to the direct beam stopper. Even the 8-layer periodicity at ±44 V (C_{8p}, Fig. 4 (i)) might be discernible, though most of the peaks had a very weak intensity. The streak pattern appeared above ±46 V (the solid line in Fig. 4 (j)) and disappeared around ±50 V (the dotted line in Fig. 4 (j)).

Fig. 5 shows the RXS peak positions as a function of the applied voltage from ±28 V to ±35 V at 83.9 °C. The main peak positions at low and high angle sides (squares) depended linearly on the voltage. Furthermore, weak subpeaks (circles) appeared at intermediate voltages from ±30 V to ±32 V and became very weak and broad at higher voltages. The subpeak positions also depended

on the voltage. It was confirmed this phenomenon did not depend on the irradiation time.

At 84.5 °C (1.0 °C above the SmC_γ^* to AF phase transition temperature and still in the AF phase), the weak stripe texture was observed at a low applied voltage (Fig. 6 (a)) and vanished gradually with increasing voltage. The RXS showed the 4-layer periodicity phase (C_{4p1}) up to ±26.0 V, as shown in Fig. 7 (a). At ±26.7 V, as the new stripe texture with the strong contrast crossed the analyzing position (Fig. 6 (b)) and the vertical chevron changed to the bookshelf structure, the weak but clear 1/2 RXS reflection appeared in addition to reflections at q/q_o = 1/4 and 3/4 (C_{4p2}) (Fig. 7 (b)), which was different from the C_{4p1} phase. At ±27.6 V, the very weak *m*/6-order reflections appeared (Fig. 7 (c)) in addition to the strong *m*/4-order reflections at the position very close to the boundary between the new homogeneous and the C_{4p2} stripe texture (Fig. 6 (c)). At ±27.8 V, the C_{4p2} state vanished at the measurement point, and very weak peaks at q/q_o = 0.85 and a weak intensity increase around q/q_o = 0.4–0.6 appeared in addition to the relatively clear peaks at q/q_o = 0.31 and 0.69 (Fig. 7 (d)). At ±28.2 V, as the homogeneous texture appeared (Fig. 6 (d)), four peaks could be recognized and assigned to the *m*/7-order reflections (Fig. 7 (e)), although the peaks at q/q_o = 1/7 and 6/7 were not observed (C_{7p}). At ±29.2 V, five broad peaks appeared and the smallest *q* peak was at q/q_o = 0.275 which was slightly smaller than q/q_o = 2/7. With a further increase of the applied voltage, the smallest *q* peak shifted to the smaller *q* and the larger *q* reflections disappeared (±29.6 V, Fig. 7 (g)). The streak remained at ±31 V (solid line in Fig. 7 (h))

and finally changed to the SmC^* phase at ±33 V (dotted line in Fig. 7 (h)). The subphase sequences near the field-induced phase transition from the SmC^*_γ phase to the SmC^* phase at 83.9 °C and at 84.5 °C are cleary different from those below 83.0 °C.

At 85.8 °C (0.1 °C below the AF to SmC^*_α phase transition temperature), the RXS showed *m*/4 –order reflections indicating the typical C_{4p1} phase, up to ±19.0 V (solid line in Fig. 8 (a)). Then, the 1/4 and 3/4 peaks shifted to lower and higher values of *q*, respectively, with increasing voltage (broken line in Fig. 8 (a)). The two peaks became weaker and broader around ±24.0 V (solid line in Fig. 8 (b)), and no other clear peaks were observed. The phase transition to the SmC^* phase occurred around ±39.0 V. Fig. 9 shows the peak positions as a function of the applied voltage (squares).

At 86.0 °C (0.1 °C above the phase transition temperature), the RXS pattern had two peaks without any electric field. These two peaks were difficult to assign to the simple integer periodic structure (Fig. 8 (c)). The lower peak positions decreased in *q*, which indicated an increase of the layer periodicity, with increasing temperature as shown in Fig. 10; the phase that appeared above the AF phase in this sample was confirmed to be the SmC^*_α phase. The voltage dependence of the peak position at 86.4 °C in Fig. 9 (circles) showed the gradual increase of the layer periodicity above ±15 V followed by the sharp increase in the higher voltage.

IV. Discussion

The transitional subphases appeared near the field-induced transition to the ferroelectric phase at the specific temperature and voltage. It is noted that the transitional subphases newly observed in the present experiment were recognized by the texture change or the weak boundary line with the *in-situ* optical microscope regardless of whether X-rays irradiated the sample or not. The experimental results are summarized as a function of the applied electric field and temperature (*E-T* diagram) in Fig. 11. The major phases, such as the C_{2p} (SmC_A^*), C_{3p} (SmC_γ^*), C_{4p1} (AF), SmC_α^* and SmC^* (Ferro) phases, are confirmed to be the same as those already reported for various LCs [2, 10-16, 27-35]. The molecular arrangements of two types of newly observed transitional subphases, namely the $C_{\nu p}$ subphases (ν = 4 through 7) and the subphases that show the peak shifts from the conventional $C_{\nu p}$ peak positions, are discussed below based mainly on the RXS theory [40, 41].

First, the $C_{\nu p}$ subphases (ν = 4 through 7) are discussed semi-quantitatively. From 81.6 °C to 83.0 °C, near the field-induced phase transition from the C_{3p} phase to the SmC^* phase, the intensities of the C_{3p} peaks became weaker and the peaks associated with the C_{6p} subphase appeared. Since neither considerably strong nor weak peaks were observed in the C_{6p} subphase (e.g., solid line in Fig. 2 (d)), the five peaks are considered to have nearly equal intensities (note that experimental conditions were optimized for the 2/6 reflection). In contrast, the previously reported C_{6p} layer

structures provided the strong 1/6 and 5/6 reflections [22, 25]. The Ising (flat), distorted clock, and (perfect) clock models [3] were examined to analyze the molecular arrangement of this new C_{6p} subphase. For the distorted clock model, the distortion angle (δ) is defined as the smallest rotation angle of the director between two successive layers in the C_{6p} subphase. Figs. 12 (a) to (e) show the RXS reflection intensities as a function of δ starting from the five independent Ising configurations at δ = 0° and Fig.12 (e) represents the intensities for the distorted synclinic configuration. Figs.12 (a), (b), (d) and (f) at δ = 60° correspond to the clock model. Since the molecules in the antiferroelectric state were reported to align parallel to the electric field [45], the intensities corresponding to the 90° azimuthal rotation of the molecules are also shown in Fig. 12 (d) and (e) as dotted lines. From Fig. 12, the molecular orientation $\{R^5L\}$ ({RRRRRL}) with a small value of δ provides the nearly equal intensity reflection pattern, where {…} represents the molecular configuration in a unit cell, and "R" and "L" indicate the smectic layer with directors tilted to the right and left, respectively. Other models do not agree with the experimental results: Figs. 12 (b), (d), and (f) show very weak (forbidden) reflections, and Figs. 12 (c) and (e) produce strong reflections. The distorted clock modification of the anticlinic {RLRLRL} configuration had the strong 1/2 reflection as expected (not shown here). Furthermore, q_E = 2/3 of the $\{R^5L\}$ configuration, where $q_E = |[R] - [L]|/([R] + [L])$, [R] and [L] are the number of "R" and "L" layers in a unit cell [3, 31], is a reasonable layer structure of the subphase appearing between the C_{3p} (q_E =

1/3) and Sm C^* (q_E = 1) phases. From these considerations, the C_{6p} subphase observed here is close to the $\{R^5L\}$ configuration with a relatively small value of δ, however, the more complicated distorted C_{6p} structures cannot be ignored.

The 7-layer periodicity subphase has not been observed by the RXS experiment. Eight independent Ising configurations for the C_{7p} subphase (e.g., Fig. 2(g)) are expected; however, it is complicated to calculate several types of distorted clock models. Furthermore, the experimentally obtained intensities were weak for a detailed discussion. Nevertheless, the $\{R^6L\}$(q_E = 5/7) and $\{R^3LRL^2\}$(q_E = 1/7) structures with a small value of δ were confirmed to provide a nearly equal intensity reflection pattern. However, $\{R^6L\}$ is likely to be realized, considering the q_E values of both models. In summary, the C_{6p} and C_{7p} subphases have the $\{R^5L\}$ and $\{R^6L\}$ configuration, respectively, with relatively small value of δ, and, at these temperatures, the C_{3p} $\{R^2L\}$ phase directly transforms to the C_{6p} $\{R^5L\}$ subphase and then to the C_{7p} $\{R^6L\}$ subphase.

At 83.9 °C, the subphases of the 5-, 6-, and 7- (8-) layer periodicities ($C_{\nu p}$, ν = 5 to 7 (8)) appeared above ±38.0 V. There has been no report about the 5-layer periodicity subphase by the RXS experiment. The C_{5p} subphase (Fig. 4 (f)) had m/5-order reflections of nearly equal intensities. Figs. 13 (a) to (c) shows the satellite reflection intensities starting with the three independent C_{5p} Ising structures as a function of δ, and Fig. 13 (d) represents the intensities for the distorted synclinic structure. Since Figs. 13 (b), (c) and (d) have weak reflections, the configuration shown in Fig. 13

(a) seems to explain the experimental results of the C_{5p} subphase, i.e., the $\{R^4L\}$ configuration with a relatively small value of δ. The RXS reflection patterns of the C_{6p} (±40V, Fig. 4(g)) and C_{7p} (±42V, Fig. 4(h)) subphases are similar to those in Fig. 2 (d) (solid line) and (g) at 81.6 °C, respectively. Taken together, the $C_{\nu p}$ (ν = 5 through 7) subphases at 83.9 °C are close to the $\{R^{\nu-1}L\}$ (ν = 5 through 7) configuration with a small value of δ.

At 84.5 °C, the weak 2/4 reflection appeared in addition to the1/4 and 3/4 reflctions at ±26.7 V and at ±27.6 V (C_{4p2}). The C_{4p1} configuration is the SmC^*_{d4} structure [13, 14], i.e. the distorted {RRLL} configuration, in which the 2/4 reflection is forbidden for $\sigma\pi$ ($\pi\sigma$) scattering, as shown in Fig.14 (a). Fig. 14 (b) shows the reflection intensities of the distorted clock configuration starting with the $\{R^3L\}$ arrangement as a function of δ. Considering the relatively weak 2/4 reflection intensity in Fig. 7 (b) and (c), the C_{4p2} state can be explained by the configuration shown in Fig. 14 (b) with a relatively large value of δ. At 84.5 °C, in contrast to the results at 83.9 °C, neither clear C_{3p} phase nor the C_{5p} subphase were confirmed, though very weak peaks at q/q_o = 1/3 (or 2/6) were observed at ±27.6 V. At 83.9 °C and at 84.5 °C, the characteristic sequential transition, i.e., AF → SmC^*_γ (C_{3p}) → SmC^* [3, 29], takes place and the temperature 84.5 °C is close to the critical point where the C_{3p} phase disappears in the *E*-*T* diagram. The novel C_{4p2} subphase and other transitional subphases at 84.5 °C may be related to this complicated situation.

The effect of the optical pitch has not been discussed for the analysis of the transitional

subphases so far. Although, it was not decided experimentally whether there was the helical structure in the transitional subphase, the introduction of the long optical pitch practically modified the δ dependencies discussed above. However, the same conclusion was deduced within a framework of the semi-quantitative analysis.

As explained in the "Experimental results" section, multiple RXS peaks more than two were not observed in the major phases, i.e. C_{2p}, C_{3p}, C_{4p1}, SmC^*_α, and no peak was observed in the SmC^* phase. However, the weak higher-order peaks in the SmC^*_α and SmC^* phases due to the helical structure were reported in the RXS experiment [11]. The higher-order peak (*m/p*) reported in practice had usually much weaker intensity compared to the fundamental one just because it was due to the helical structure. Since the present experimental results discussed here were different from those intensity profiles, the new $C_{\nu p}$ phase does not form the simple helical structure.

To summarize, the new $C_{\nu p}$ subphases (ν = 4 through 7) observed near the field-induced phase transition from the C_{3p} to SmC^* phases are the distorted $\{R^{\nu-1}L\}$ (ν = 4 through 7) configurations. These configurations are also reasonable from the view of the q_E value, i.e., $q_E = (\nu-2)/\nu$ and hence they suggest how the field-induced phase transition proceeds. The $\{R^{\nu-1}L\}$ configuration in the presence of electric field, however, has been hardly discussed. The *E-T* diagram analyzed by Dolganov et al. [46] was successful for explaining the 5-layer and 6-layer periodicity phases, but

their molecular configurations were different from the present structures. The recent theoretical approach proposed the long-periodicity ferrielectric phases [39]; however, the $\{R^{\nu-1}L\}$ configuration was not found in the calculated results. In the analysis of the long-periodicity subphase by Chandani et al. [40], the C_{6p} $\{R^5L\}$ structure appeared as one of the possible configurations in the electric-field induced phase transition. The superlattice structures recently proposed [47] might coincide with our transitional subphases (q_E = 1/2 and 3/5 for C_{4p2} and C_{5p}, respectively), though the sample, the experimental conditions were different from our experiments. The C_{4p2} $\{R^3L\}$ configuration was once discussed theoretically [44] as one of the two possible 4-layer periodicity. Thus, the physical origin of the $\{R^{\nu-1}L\}$ configuration under the electric field remain unsolved.

The single uniform subphases were assumed in the present analysis; however, the coexistence of the micro-domains cannot be denied in some subphases. The configuration models examined here are based on the semi-quantitative discussions, and hence higher precision experiments are needed to confirm the details of the configurations.

The transitional subphases sometimes showed a shift of the RXS peak position ("PS" in Fig. 11) from those expected for the conventional $C_{\nu p}$ structures. Three representative peak-shift phenomena are discussed in the following: the peak-shift from C_{3p} to C_{4p} (Fig. 5), from C_{6p} to C_{7p} (Figs. 2 and 7), and from C_{4p1} to the longer periodicity near the AF and SmC^*_α transition (Fig. 9). As working models, two molecular arrangements are examined below to explain the peak position

shift from C_{3p} to C_{4p} (PS(3/4) state hereafter) in Fig. 5 at 83.9 °C: the helical modification of the C_{3p} configuration (helical model) and the appearance of a large unit cell structure (large unit cell model). From the view point of the diffraction pattern, the PS(3/4) state as a function of the electric field is similar to the peak position change as a function of temperature in the SmC^*_α phase which has a uniaxial short pitch helical structure [10, 15, 16, 18, 29]. It is noted that the helical structure generates the split of the RXS peaks. The intensity ratio and the separation of these two peaks depend on the distortion angle δ and the helical pitch, respectively: a pair of equal intensity peaks and a single peak for the Ising and (uniaxial) perfect clock models, respectively [12, 23, 42]. If the helical modification of the C_{3p} configuration, as inferred from the SmC^*_α configuration, is realized in the PS(3/4) state, the modified C_{3p} configuration should have a relatively large distortion angle because only two peaks appeared in Fig. 5 at the low applied field (±28 V and ±29 V). However, the optical biaxiality [3] and the distorted clock structure [13] were reported for the C_{3p} phase; therefore, the helical model is not fully rationalized at present. Recently, the new 3-layer periodicity phase under the electric field between the SmC^*_γ and SmC^* phases was proposed [33-35, 37]. However, it is not sure whether the new 3-layer periodicity phase affected the present results within our experimental conditions, because the RXS 1/3-order peak position does not depend on those configuration models.

Furthermore, it is difficult to explain the additional subpeaks appearing around ±30 V using the

helical model alone. These RXS peaks could be explained by the commensurate long periodicity structure (large unit cell). Since the PS(3/4) state appeared between the C_{3p} and C_{4p} phases, one of the candidates for the unit cell is the combination of the distorted C_{3p} and C_{4p} structures, i.e., (C_{3p}^{i}, C_{4p}^{j}), where i and j are the number of C_{3p} and C_{4p} blocks in the unit cell, respectively. With this model, the main and subpeaks appeared at $q/q_o = 1 / (3 + r)$ and $(1 + r) / (3 + r)$, respectively, where $r = j/(i + j)$. For example, the main peaks and subpeaks around ±30 V in Fig. 5 were reproduced by the structures with (C_{3p}^{2}, C_{4p}^{1}) 20and (C_{3p}^{3}, C_{4p}^{1}) with a relatively large value of δ. However, the large unit cell model does not seemed to be successful to explain the RXS peaks near $q/q_o = 1/3$ and 1/4, because the unit cell becomes very large (a few tens of layer). Therefore, the large unit cell structure, if it would be appropriate, may be realized only around the intermediate voltage region.

To explain the deviation of the peak positions from the ideal 6-layer periodicity in Figs. 2 (e) and (f), and in Fig. 7(d), the two structure models are examined again. If the helical modulation is introduced to the distorted clock C_{6p} phase with a small value of δ in a low field, a pair of peaks corresponding to the helical pitch should be observed. In contrast, if the nearly perfect C_{6p} clock structure with a helical modulation is realized, the lowest order peak alone would be observed [12, 23, 42]. Hence, the experimental results do not agree with either helical model.

One of the possible candidates for the intermediate state based on the large unit cell is the combination of the C_{6p} and C_{7p} blocks, i.e., (C_{6p}^{i}, C_{7p}^{j}) configuration. For example, the calculated

intensity patterns for (C_{6p}^{4}, C_{7p}^{1}) and (C_{6p}^{2}, C_{7p}^{2}) accounted for the experimental reflection intensities in Fig. 2(e) and (f), respectively. However, the calculation with slightly different values of *i* and *j* also provided the similar results within our experimental precision. The molecular arrangement in Fig. 7 (d) at 84.5 °C is considered to be close to the configurations discussed here because of the similarity of the diffraction patterns between Fig. 2 (f) and Fig. 7 (d).

The helical and large unit cell models are not fully successful for explaining the peak position shift from the conventional commensurate structure; therefore, further discussion is required in order to establish these working models.

Near the AF to SmC_{α}^{*} phase transition, the voltage dependence of the peak position in Fig. 9 (circles) indicates an increase of the helical pitch due to the electric field (unwound process) because the SmC_{α}^{*} phase at 86.0 °C was assigned to the short pitch helical structure (Fig. 10). The slope changes around ±15 V, however, and it suggests that the different states exist in the SmC_{α}^{*} phase. In contrast, from the RXS view point, the peak-shift above ±19 V at 85.8 °C (AF) may be due to the development of a SmC_{α}^{*}-like helical structure from the C_{4p1} (SmC_{d4}^{*}) phase because only two peaks appeared. The staircase-like character [47], however, cannot be excluded because of the limited number of measurement points in the present experiment.

The RXS peaks in the transitional subphases, especially when there is more than 6-layer periodicity, were usually weak and broad compared to the major phases. This is likely either due to

the small coherent region of the transitional subphase, i.e., the small grain size, or due to the statistical fluctuation of the molecular arrangement. The broad peak is not due to the large strain because no conspicuous degradation of the layer structure were observed in the ω-angle intensity profile or in the peak position of the Bragg reflection as stated in the " Experimental" section. The "streak," which was usually observed just below the transition to the SmC^* phase, can be explained either by the random distribution of the director or by the tail part of the peak at smaller values of q, i.e., the very long periodicity. The director random distribution, which is caused by the coexistence of many possible configurations, is plausible just below the transition to the SmC^* phase. A very long periodicity structure might be less preferable because the low-q peak became very weak and broad before the streak appeared.

The Br-containing LCs in our previous experiment showed a 12-layer periodicity state near the field-induced C_{3p} to SmC^* phase transition without other periodicity subphases [38], while several new transitional subphases were observed in the present Se-containing sample, except for the 12-layer periodicity. Both samples had nearly the same *E-T* phase diagram, except that the high temperature phases were SmC^* and SmC^*_α for the Br- and Se-containing LCs, respectively. The direct C_{3p} to C_{6p} and C_{3p} to C_{12p} phase transitions occurred in the Se-containing LC in the low temperature region (below 83 °C) and in the Br-containing LC, respectively. The present C_{6p} $\{R^5L\}$ configuration is realized by flipping one molecule in every other C_{3p} block, while the C_{12p}

$\{R^2LR^2LR^6\}$ configuration is realized by flipping two molecules in four C_{3p} blocks. This suggests a difference and a similarity in the interaction process and strength between the Se- and Br-containing LCs, especially in the phase at the lower electric field.

V. Conclusion

New transitional subphases in the electric field-induced phase transition of a Se-containing chiral LC in a planar aligned cell geometry were found by RXS. At lower temperatures (the SmC_A^* and SmC_γ^* phases), the C_{6p} structure and a streak pattern appeared with increasing applied electric field near the field-induced C_{3p} to SmC^* phase transition. At the higher temperatures (AF phase), the RXS peak position of the C_{3p} structure shifted to the C_{4p} structure almost continuously, and then the 5- to 7-layer periodicity subphases appeared in sequence followed by the streak pattern with increasing electric field. Furthermore, near the AF to SmC_α^* phase transition, the RXS peak continuously shifted to a longer periodicity with applied voltage. The molecular configurations of the new $C_{\nu p}$ (ν = 4 to 7) subphases were explained by the distorted $\{R^{\nu-1}L\}$ configuration models, while the "peak-shift" could not be fully understand by the helical or large unit cell models. The transitional subphases appeared at the specific temperature in a relatively narrow voltage range; therefore, subphases might be found using a higher precision experiment. Though the present analysis was performed from the X-ray diffraction point of view, the understanding of the physical origin of the field-induced subphases is important for the studies of the rich variety of subphases

appearing in the chiral smectic LCs and is one of the future problems to be solved in this research field.

Acknowledgements

The authors would like to thank Ms. Y. Ohtsuka and the staff of the Photon Factory for their help during the experiments. This work was carried out under the approval of the Photon Factory Advisory Committee (Proposal Nos. 2012G635 and 2014G638). This work was partly supported by the Grant-In-Aid for Scientific Research on Priority Area (A) (23246007) of the Ministry of Education, Culture, Sports, Science and Technology. Work of the Dublin group was supported by Ireland-Japan International Strategic Cooperation Award and partly by 13/US/I2866 from the Science Foundation of Ireland as US–Ireland Research and Development Partnership program administered jointly with the United States National Science Foundation under grant number NSF-DMR-1410649.

References

[1] S. T.Lagerwall, *Ferroelectric and Antiferroelectric Liquid Crystals* (Wiley, Weinheim, 1999).

[2] H. Takezoe, E. Gorecka and M. Čepič, Rev. Mod. Phys., **82**, 897 (2010).

[3] A. Fukuda, Y. Takanishi, T. Isozaki, K. Ishikawa, and H. Takezoe, J. Mater. Chem.**4**, 997 (1994).

[4] A. D. L. Chandani, E. Gorecka, Y. Ouchi, H. Takezoe, and A. Fukuda, Jpn. J. Appl. Phys. **28**, L1265 (1989).

[5] T.Isozaki, T.Fujikawa, H.Takezoe, A.Fukuda, T.Hagiwara, Y.Suzuki and I.Kawamura, Phys. Rev. B **48**, 13439 (1993).

[6] Yu.P.Panarin, O.Kalinovskaya, J.K.Vij and J.W.Goodby, Phys. Rev.E **55**, 4345 (1997).

[7] K. Itoh, M. Kabe, K. Miyachi, Y. Takanishi, K. Ishikawa, H. Takezoe and A. Fukuda, J. Mater. Chem., **7**, 17 (1997).

[8] M. Yamashita, Ferroelectrics **181**, 201 (1996).

[9] M.Yamashita and S.Tanaka Jpn. J. Appl. Phys. **37**, L528 (1998).

[10] P. Mach, R. Pindak, A. M. Levelut, P. Barois, H. T. Nguyen, C. C. Huang, and L. Furenlid, Phys. Rev. Lett. **81**, 1015 (1998).

[11] L. S. Hirst, S. J. Watson, H. F. Gleeson, P. Cluzeau, P. Barois, R. Pindak, J. Pitney, A. Cady, P. M. Johnson, C. C. Huang, A. M. Levelut, G. Srajer, J. Pollmann, W.Caliebe, A. Seed, M. R. Herbert,

J. W. Goodby, and M. Hird, Phys. Rev. E **65**, 041705 (2002).

[12] A. Cady, J. A. Pitney, R. Pindak, L. S. Matkin, S. J. Watson, H. F. Gleeson, P. Cluzeau, P. Barois, A.-M. Levelut, W. Caliebe, J. W. Goodby,M. Hird, and C. C. Huang, Phys. Rev.E **64**, 050702 (2001)

[13] N. W. Roberts, S. Jaradat, L. S. Hirst, M. S. Thurlow, Y. Wang, S. T. Wang, Z. Q. Liu, C. C. Huang, J. Bai, R. Pindak and H. F. Gleeson, Europhys. Lett. **72**, 976 (2005).

[14] P.D. Brimicombe, N.W. Roberts, S. Jaradat, C. Southern, S.-T. Wang, C.-C. Huang, E. DiMasi, R. Pindak, and H.F. Gleeson, Eur. Phys. J. E **23**, 281 (2007).

[15] A. Cady, D. A. Olson, X. F. Han, H. T. Nguyen, and C. C. Huang, Phys. Rev. E **65**, 030701 (2002).

[16] Z. Q. Liu, B. K. McCoy, S. T. Wang, R. Pindak, W. Caliebe, P. Barois, P. Fernandes, H. T. Nguyen, C. S. Hsu, S. Wang, and C. C. Huang, Phys. Rev. Lett. **99**, 077802 (2007).

[17] M. A. Osipov, A. Fukuda, and H. Hakoi, Mol. Cryst. Liq. Cryst. **402**, 9 (2003).

[18] A. V. Emelyanenko and M.A.Osipov, Phys. Rev. E **68**, 051703 (2003).

[19] P. V. Dolganov, V. M. Zhilin,V.K.Dolganov and E. I. Kats, Phys. Rev. E **67**, 041716 (2003).

[20] M.B.Hamaneh and P.L.Taylor, Phys. Rev.Lett. **93**, 167801 (2004).

[21] P. V. Dolganov, V. M. Zhilin, and E. I. Kats, *J. Exp. Theor. Phys.*, **115**, 1140 (2012).

[22] S. Wang, L. D. Pan, R. Pindak, Z. Q. Liu, H. T. Nguyen, and C. C. Huang, Phys. Rev. Lett. **104**,

027801 (2010).

[23] L.D.Pan, R.Pindak and C.C.Huang, Phys. Rev. E **89**, 022501 (2014).

[24] C.C. Huang, Shun Wang, LiDong Pan, Z.Q. Liu, B.K. McCoy, Yuji Sasaki, Kenji Ema, P. Barois and Ron Pindak, Liquid Crystal Reviews **3**, 58 (2015).

[25] Y. Takanishi, I. Nishiyama, J. Yamamoto, Y. Ohtsuka and A. Iida, Phys. Rev. E **87**, 050503(R) (2013).

[26] Y.Takanishi, Y.Ohtsuka, Y.Takahashi, S.M.Kang and A.Iida, Eur. Phys. Let. **109**, 56003 (2015).

[27] K. Hiraoka, Y.Takanishi, K.Skarp, H. Takezoe, and A. Fukuda, Jpn. J. Appl. Phys. **30**, L1819 (1991).

[28] K.Hiraoka, A.Taguchi, Y.Ouchi, H.Takezoe, A.Fukuda, Jpn. J. Appl. Phys. **29**, L103 (1990).

[29] N. M. Shtykov, J. K. Vij, R. A. Lewis, M. Hird, and J. W. Goodby, Phys. Rev. E **62**, 2279 (2000).

[30] A. D. L. Chandani, N. M. Shtykov, V. P. Panov, A. V. Emelyanenko, A. Fukuda, and J. K. Vij, Phys. Rev. E **72**, 041705 (2005).

[31] K. L. Sandhya, A. D. L. Chandani, A. Fukuda, S. Kumar, and J. K. Vij, Phys. Rev. E **87**, 062506 (2013).

[32] L. S. Matkin, S. T. Watson, H. F. Gleeson, R. Pindak, J. Pitney, P. M. Johnson, C. C. Huang, P.

Barois, A. M. Levelut, G. Srajer, J. Pollmann, J.W.Goodby and M.Hird, Phys. Rev. E **64**, 021705 (2001).

[33]S. Jaradat, P. D. Brimicombe, C. Southern, S. D. Siemianowski, E. DiMasi, M. Osipov, R. Pindak, and H. F. Gleeson, Phys. Rev. E **77**, 010701 (2008).

[34] S. Jaradat, P. D. Brimicombe, M. A. Osipov, R. Pindak and H. F. Gleeson, App. Phys. Lett. **98**, 043501 (2011).

[35] H. F. Gleeson, S. Jaradat, A. Labeeb and M. Osipov, Ferroelectrics, **431**, 40 (2012).

[36]H. S. Chang, S. Jaradat, H. F. Gleeson, I. Dierking, and M. A. Osipov, Phys. Rev. E **79**, 061706 (2009).

[37] L. Johnson, S. Jaradat and H. F. Gleeson, J. Mater. Chem. C, **2**, 147 (2014).

[38] A. Iida, I. Nishiyama, and Y. Takanishi, Phys. Rev. E **89**, 032503 (2014).

[39] A.V.Emelyanenko, Ferroelectrics, **495**, 129 (2016).

[40] A. D. L. Chandani, A. Fukuda, J. K. Vij, Y. Takanishi, and A. Iida, Phys. Rev. E **93**, 042707 (2016).

[41] Y. Takanishi, Y. Ohtsuka, Y. Takahashi and A. Iida, Phys. Rev. E **81**, 011701 (2010).

[42] A.-M.Levelut and B.Pansu, Phys. Rev. E **60**, 6803 (1999).

[43] Y. Takahashi, A. Iida, Y. Takanishi, T. Ogasawara, M. Nakata, K. Ishikawa and H. Takezoe, Phys. Rev. E **67**, 051706 (2003)

[44] M. A. Osipov and M. V. Gorkunov, Liquid Crystals, **33**, 1133 (2006).

[45] L. A. Parry-Jones and S. J. Elston, Phys. Rev. E 63, 050701(R) (2001).

[46] P. V. Dolganov, V. M. Zhilin, V. K. Dolganov and E. I. Kats, Phys. Rev. E **86**, 020701 (2012).

[47] K. L. Sandhya, J. K. Vij, A. Fukuda, and A.V.Emelyanenko, Liquid Crystals **36**, 1101 (2009).

Figure Captions

Fig. 1 Sample photos observed at applied fields of (a) ±20 V, (b) ±30 V, (c) ±83.8 V, and (d) ±91 V at 81.2 °C. The layer normal was approximately horizontal. The black arrows show the phase boundary between the 2-layer periodicity phase and the 3-layer phase (b), and the boundary between the C_{7p}-like phase and the "streak" state (c). In photo (d), most of the field of view transforms to the SmC^* phase, while the streak state (elongated, island-like region) remains. In (d), the white arrow indicates the typical measurement point and the scale bar represents 0.1 mm. The blot-like patterns of various sizes and shapes are due to the contamination on the outside of the glass plate. The ω-angular profiles were obtained at ±20.0 V (e) and ±80.0 V (f). The molecular structure of the sample LC is shown at the top.

Fig. 2 A series of resonant X-ray scattering (RXS) profiles obtained at applied fields from ±10 V to ±91.0 V at 81.2 °C. In (c) and (g), thin chain dotted lines show the magnified profiles. Asterisks in (d) and (g) indicate the positions where the reflection peaks due to the C_{6p} and C_{7p} configurations, respectively, are expected to appear. The insets in (a) and (h) are the two-dimensional diffraction patterns from which the one-dimensional RXS profiles were extracted; in the inset, the white circles correspond to the shadow of the direct beam stopper, the strong arc-like spot on the right is the first-order Bragg diffraction, and a weak RXS reflection in (a) and streak in (h) (A) are seen between the direct beam stopper and the

first-order diffraction. The left (A) and right (B) insets in (h) correspond to ±85.1 V and ±91.0 V, respectively.

Fig. 3 A series of RXS profiles obtained at applied fields from ±70.8 V to ±76.0 V at 83.9 °C. The asterisks in (b) and (d) are the expected peak positions for the C_{6p} and C_{7p} configurations, respectively.

Fig. 4 A series of RXS profiles obtained at applied fields from ±18.0 V to ±52.0 V at 83.9 °C. In (b), the broken and solid lines are obtained at the first and second measurements. The asterisks in (f) through (i) are the expected peak positions for the C_{5p} through C_{8p} configurations.

Fig. 5 RXS satellite peak positions as a function of the applied voltage at 83.9 °C. Squares and circles correspond to the strong and weak peaks, respectively. Horizontal broken and dotted lines correspond to q/q_0 = 1/3 and2/3, and q/q_0 =1/4 and 3/4, respectively, for reference.

Fig. 6 Sample photos observed at fields of (a) ±15 V, (b) ±26.7 V, (c) ±27.6 V, and (d) ±28.2 V at 84.5 °C. The black arrows show the phase boundary between the two 4-layer periodicity phases (b), between the new homogeneous texture and the 4-layer state (c) and between the homogeneous texture and the 7-layer state (d). The white arrow in (c) indicates the typical measurement point.

Fig. 7 A series of RXS profiles obtained at applied fields from ±25.5 V to ±33.0 V at 83.9 °C. The

broken curves in (a)-(c) are vertically magnified intensities to show the weak peaks. The asterisks in (c) and (e) are the expected peak positions for the C_{6p} and C_{7p} configurations, respectively.

Fig. 8 A series of RXS resonant X-ray scattering profiles obtained at applied fields of (a) ±9.23 V (solid line) and ±20.3V (broken line), (b) ±24.0 V (solid line) and ±39.0V (broken line) at 85.8 °C, and (c) at 86.0 °C without an electric field.

Fig. 9 Peak positions (q/q_0) as a function of the applied voltage at 83.9 °C (squares) and 86.4 °C (circles). The right axis is the inverse of the left axis.

Fig. 10 Peak positions (q/q_0) as a function of temperature for the SmC_α^* phase without an electric field.

Fig. 11 Summary of the resonant X-ray scattering (RXS) experiments as a function of temperature and applied voltage. The circles and squares show the major field-induced phase transitions and the field-induced transitional subphases, respectively. "PS" indicates the voltage range in which the positions of the RXS peaks shift to the ones corresponding to a longer periodic structure with increasing electric field. "Streak" indicates diffuse scattering with no clear diffraction peaks along the layer normal and "Ferro" marks the region where no RXS satellite appears (SmC^*).

Fig. 12 Calculated RXS reflection intensities as a function of the distortion angle (δ) for six independent 6-layer periodicity configurations: squares, circles, and triangles show q/q_0 =1/6 and 5/6, q/q_0 = 2/6 and 4/6, and q/q_0 = 3/6, respectively. Only $\sigma\pi$ scattering is shown. Solid lines correspond to the molecular configurations shown in the insets and the incident X-rays were parallel to the electric field. Dotted lines and marks filled in white in (d) and (e) correspond to the configuration of the 90° azimuthal rotation of the molecule.

Fig. 13 Calculated RXS reflection intensities as a function of the distortion angle for 5-layer periodicity configurations. Squares and circles correspond to reflections for q/q_0 =1/5 and 4/5, and q/q_0 = 2/5 and 3/5, respectively. Incident X-rays were parallel to the electric field.

Fig. 14 Calculated RXS reflection intensities as a function of the distortion angle for 4-layer periodicity configurations: filled squares and circles correspond to reflections for q/q_0 =1/4 and 4/3, and q/q_0 = 2/4, respectively. Solid lines correspond to the molecular configurations shown in the insets and a dotted line and white circles in (a) corresponds to the configuration of the 90° azimuthal rotation of the molecule for q/q_0 =1/4 and 4/3.

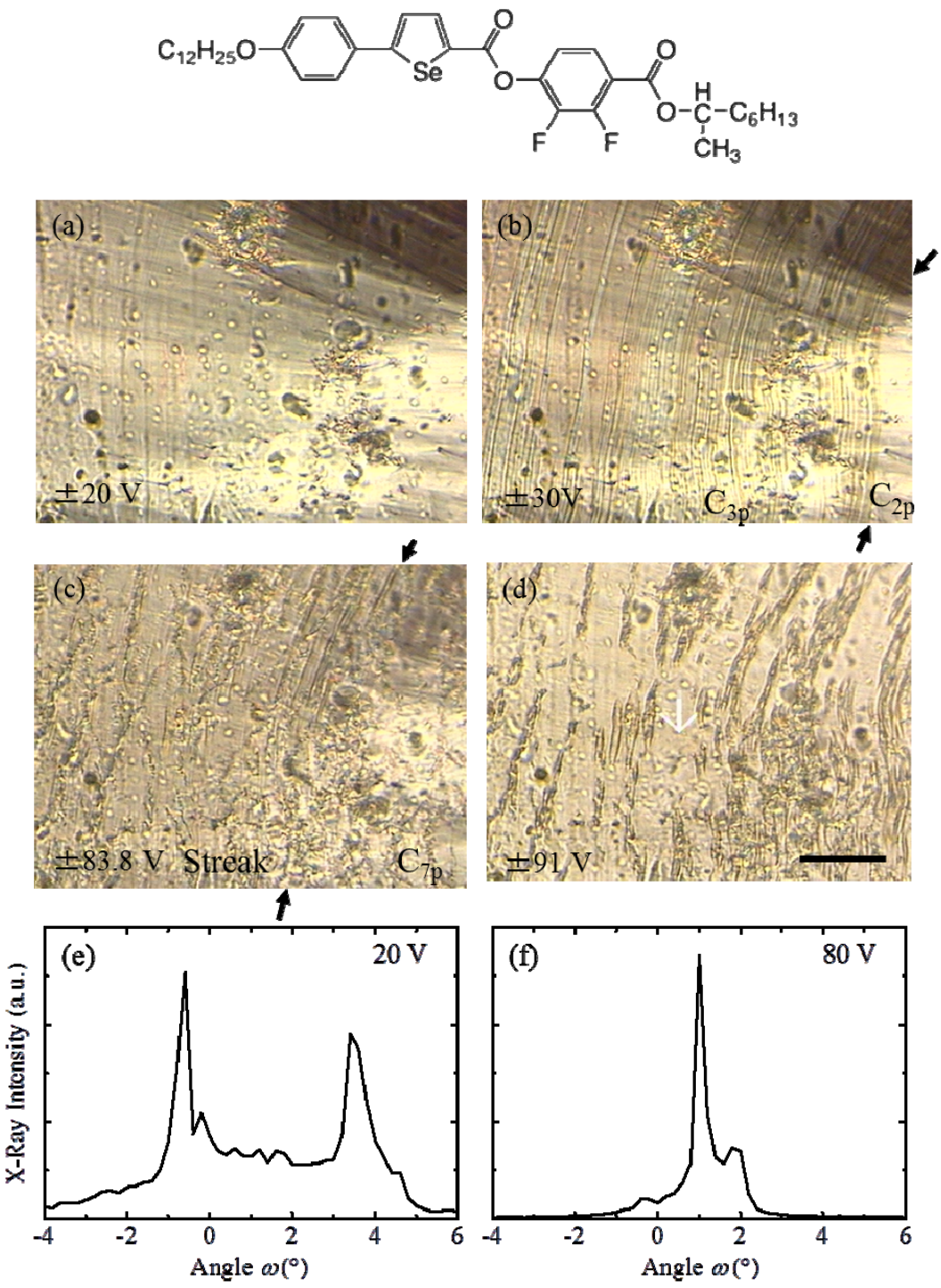
C12H25O
Se
O
O
O
O
F
F
H
C
C6H13
CH3
(a)
±20 V
(b)
±30V
C3p
C2p
(c)
±83.8 V Streak
C7p
(d)
±91 V
(e)
20 V
(f)
80 V
X-Ray Intensity (a.u.)
-4
-2
0
2
4
6
Angle ω(°)

Fig.1

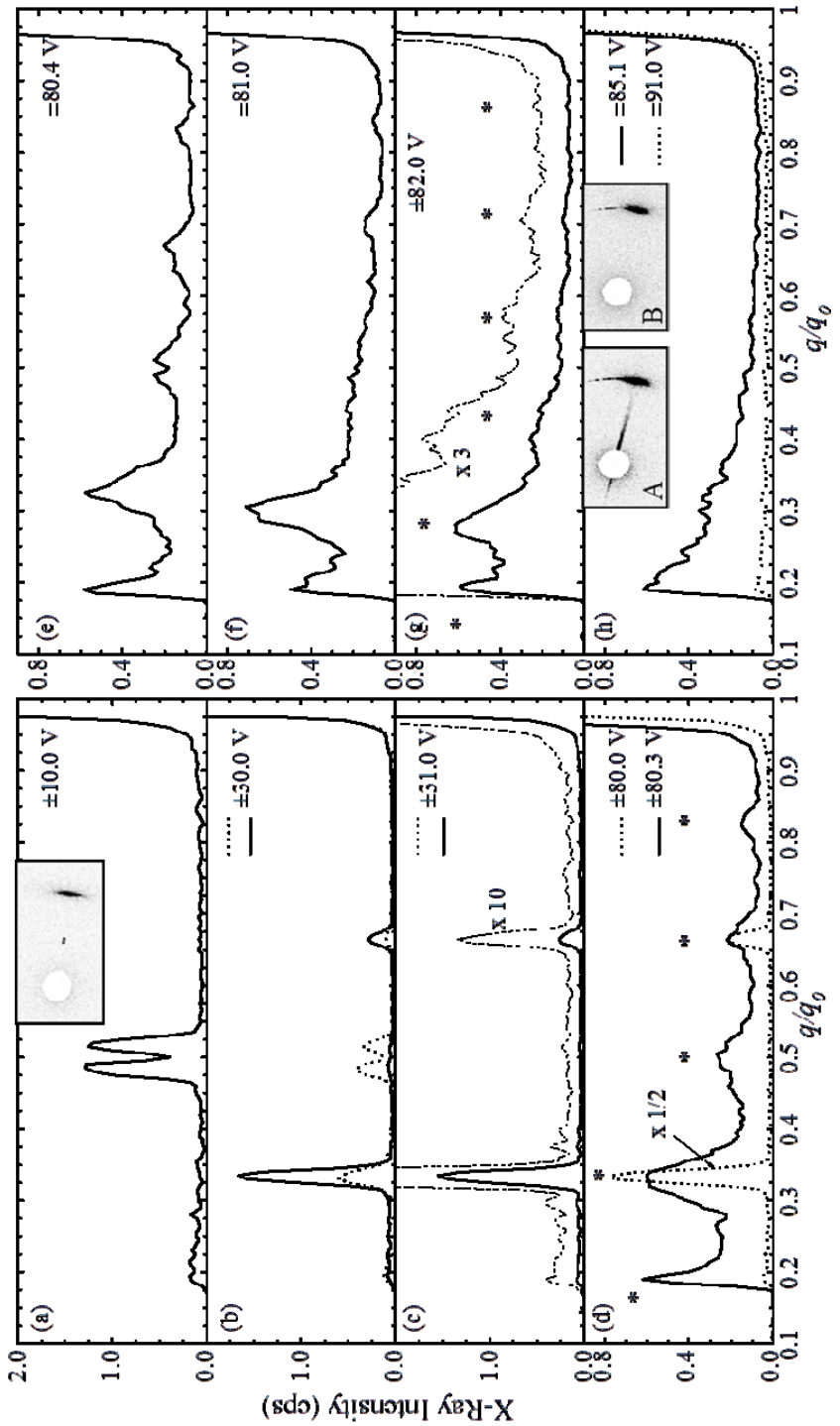
X-Ray Intensity (cps)
q/q0
(a)
±10.0 V
(b)
±30.0 V
(c)
±31.0 V
x 10
(d)
±80.0 V
±80.3 V
x 1/2
(e)
±80.4 V
(f)
±81.0 V
(g)
±82.0 V
x 3
(h)
±85.1 V
±91.0 V
A
B

Fig.2

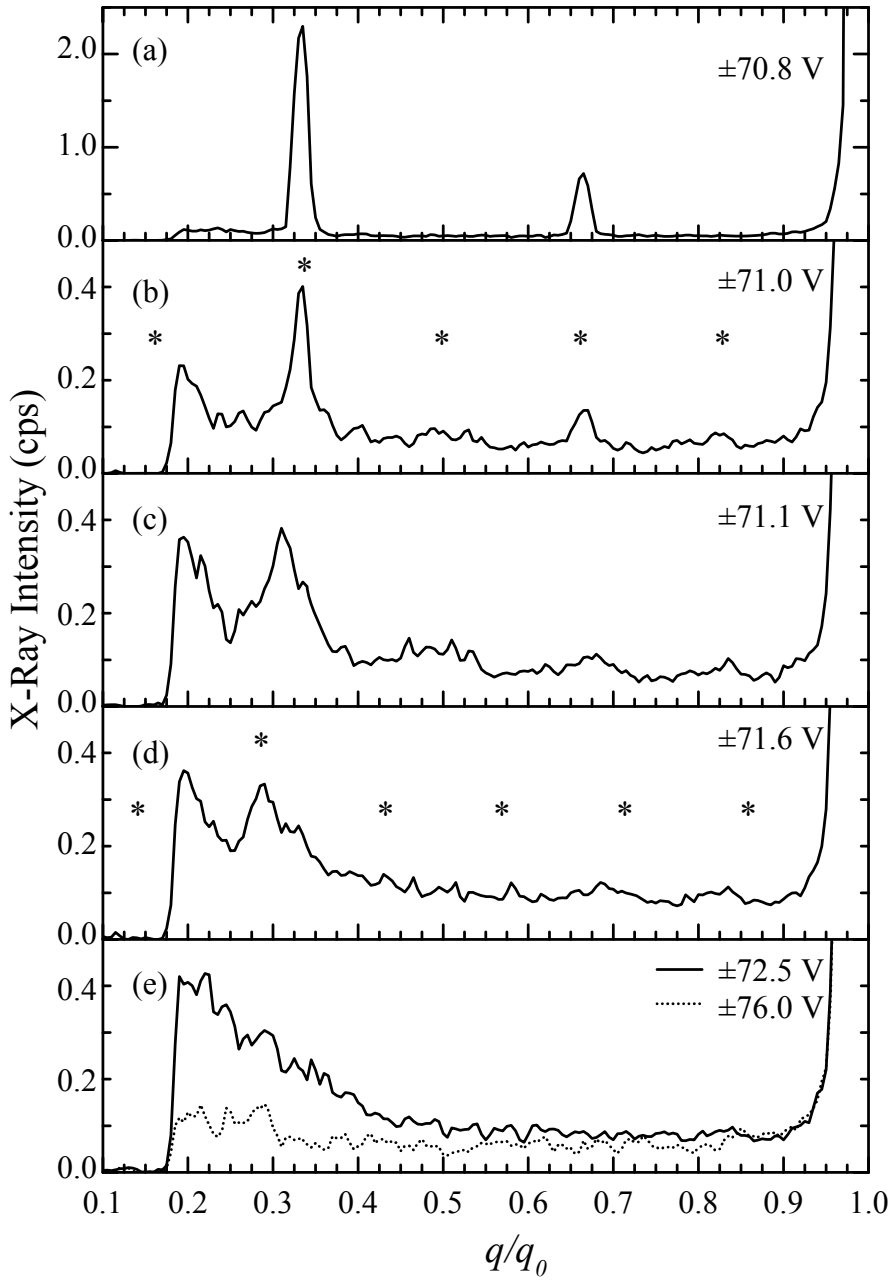

Fig.3

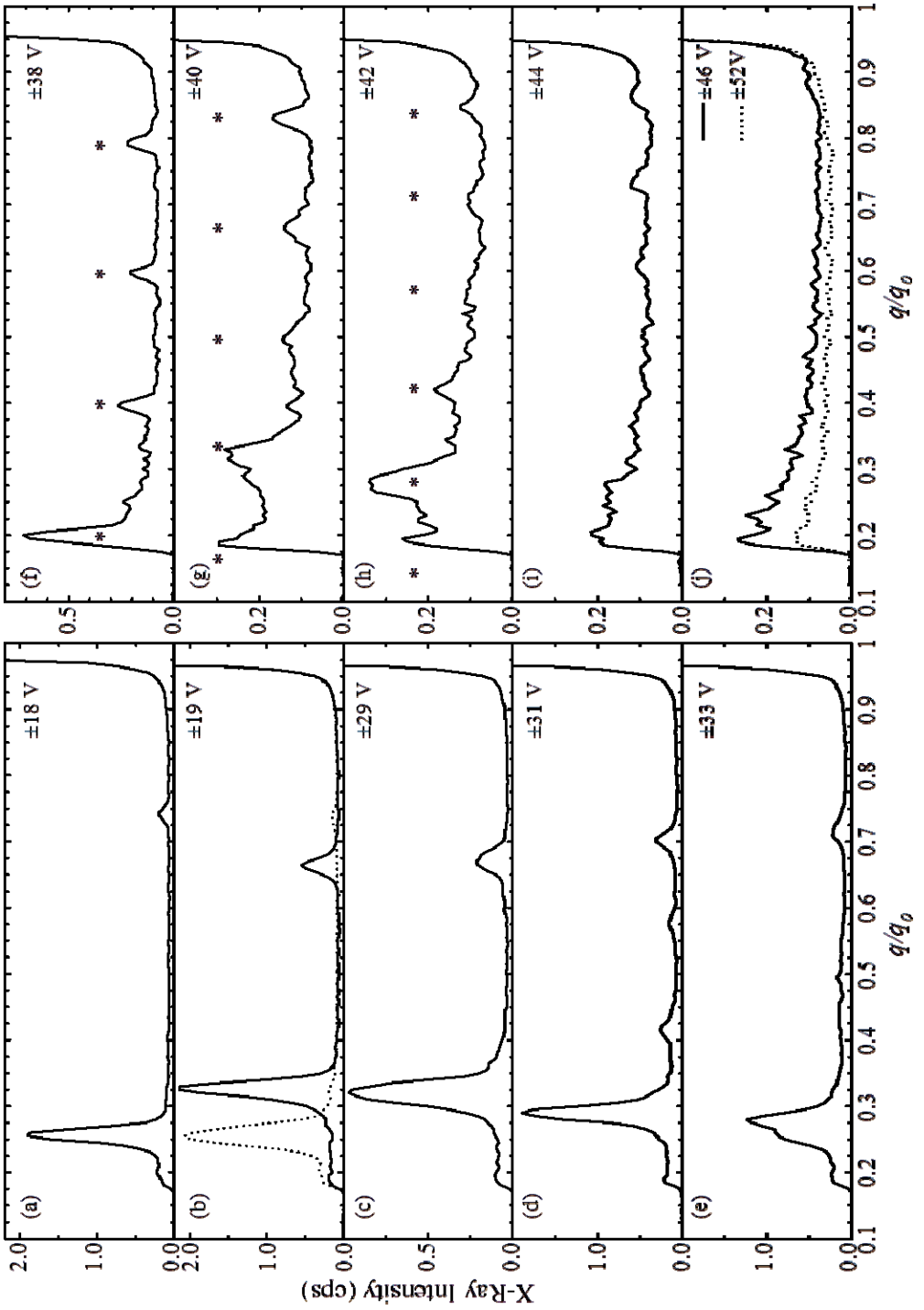
X-Ray Intensity (cps)
q/q0
(a) ±18 V
(b) ±19 V
(c) ±29 V
(d) ±31 V
(e) ±33 V
(f) ±38 V
(g) ±40 V
(h) ±42 V
(i) ±44 V
(j) ±46 V
±52V

Fig.4

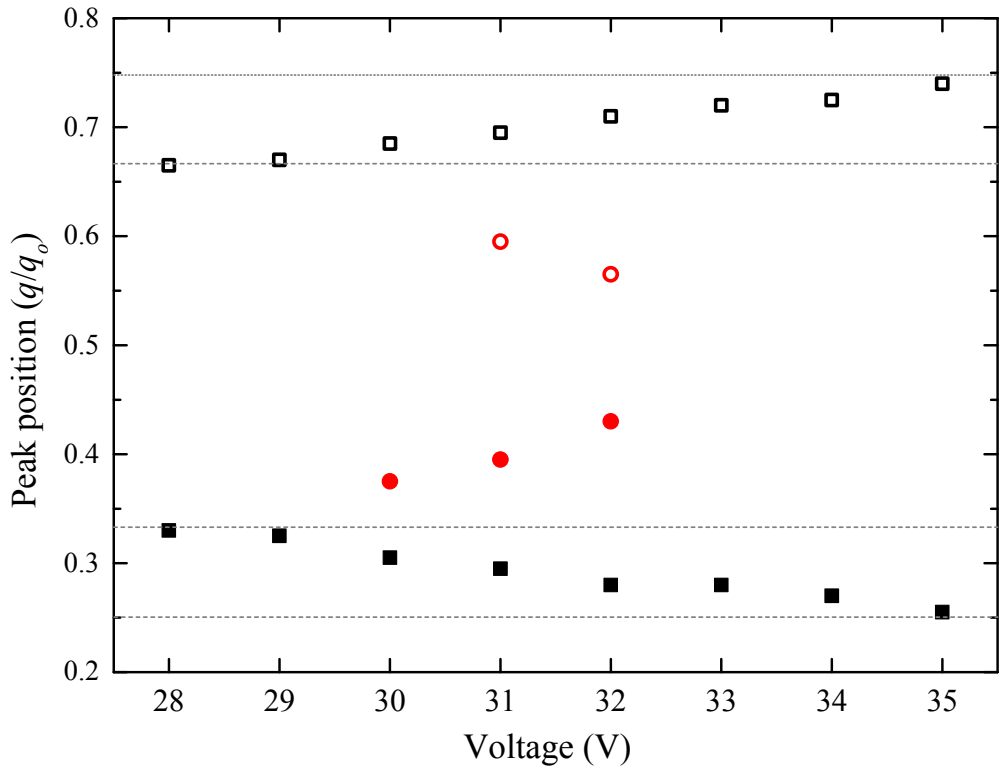
0.8
0.7
0.6
0.5
0.4
0.3
0.2
Peak position (q/q_o)
28
29
30
31
32
33
34
35
Voltage (V)

Fig.5

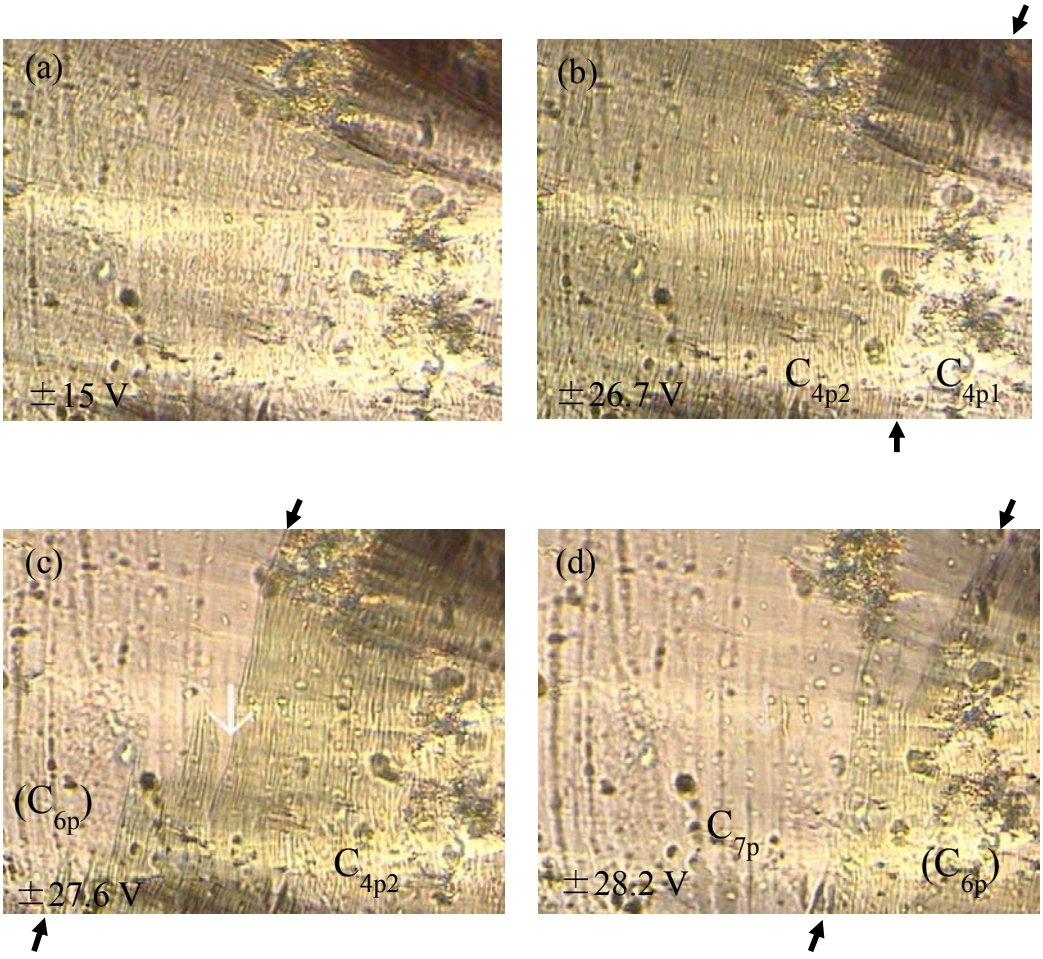

Fig.6

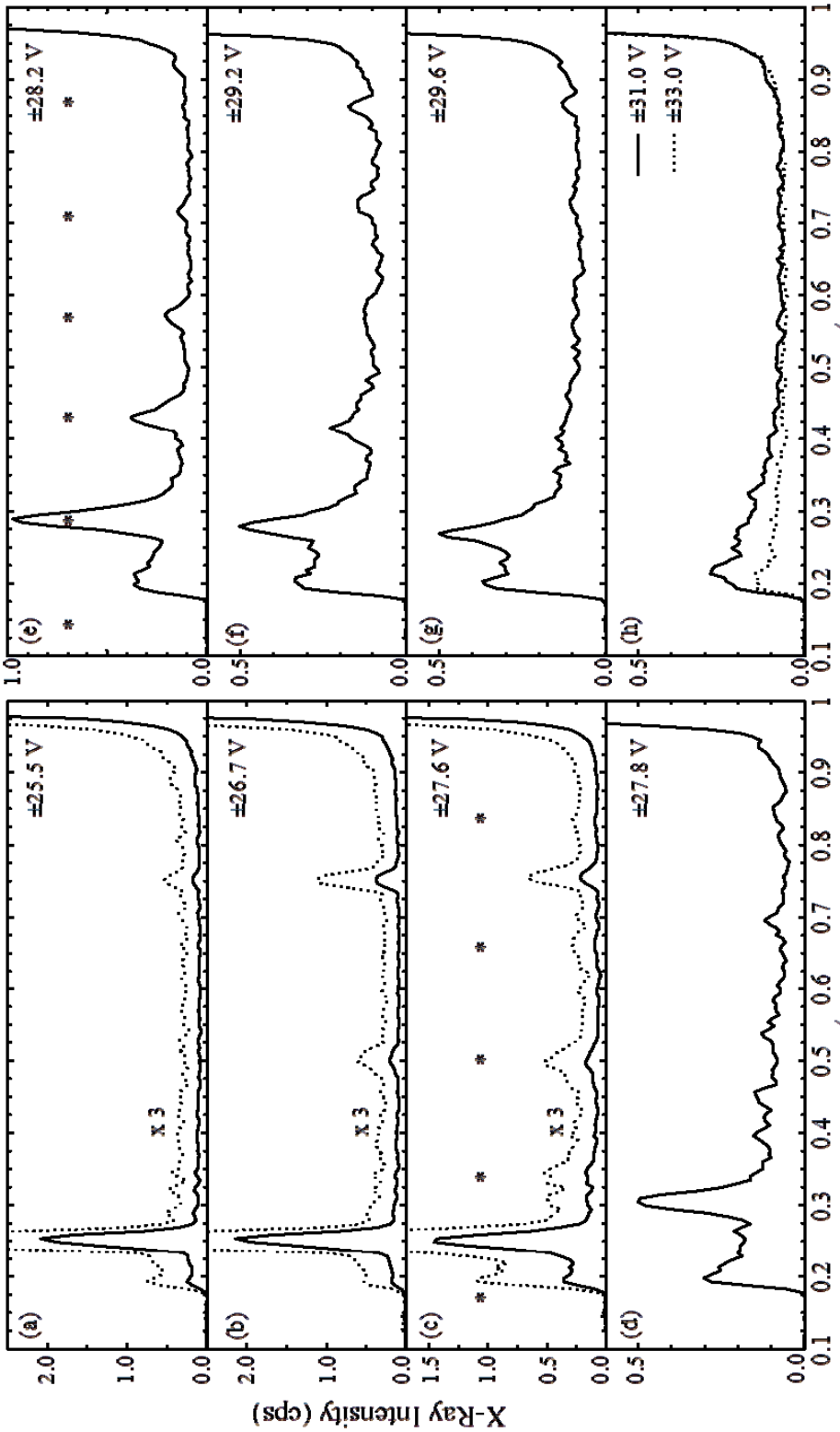
X-Ray Intensity (cps)
q/q₀
(a)
±25.5 V
x 3
(b)
±26.7 V
x 3
(c)
±27.6 V
x 3
(d)
±27.8 V
(e)
±28.2 V
(f)
±29.2 V
(g)
±29.6 V
(h)
±31.0 V
±33.0 V

Fig.7

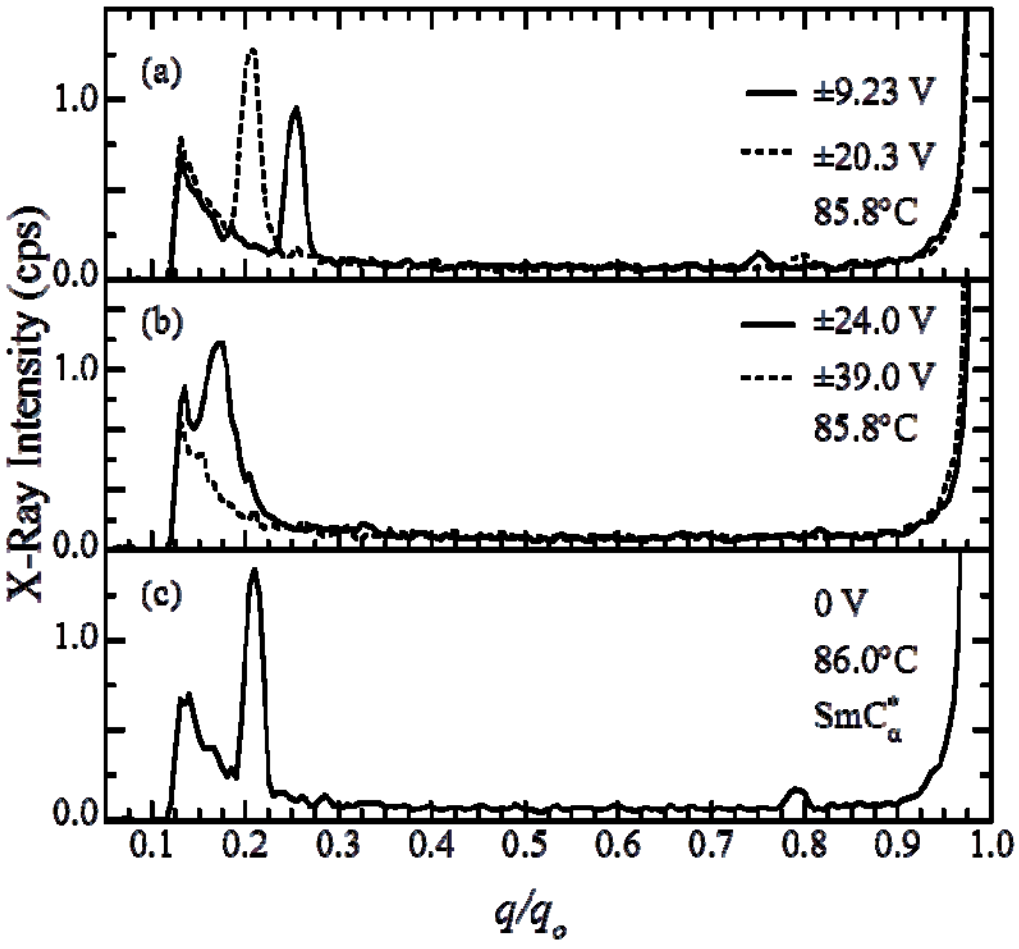
(a)
±9.23 V
±20.3 V
85.8°C
(b)
±24.0 V
±39.0 V
85.8°C
(c)
0 V
86.0°C
SmC*α
X-Ray Intensity (cps)
1.0
0.0
0.1
0.2
0.3
0.4
0.5
0.6
0.7
0.8
0.9
1.0
q/q_o

Fig.8

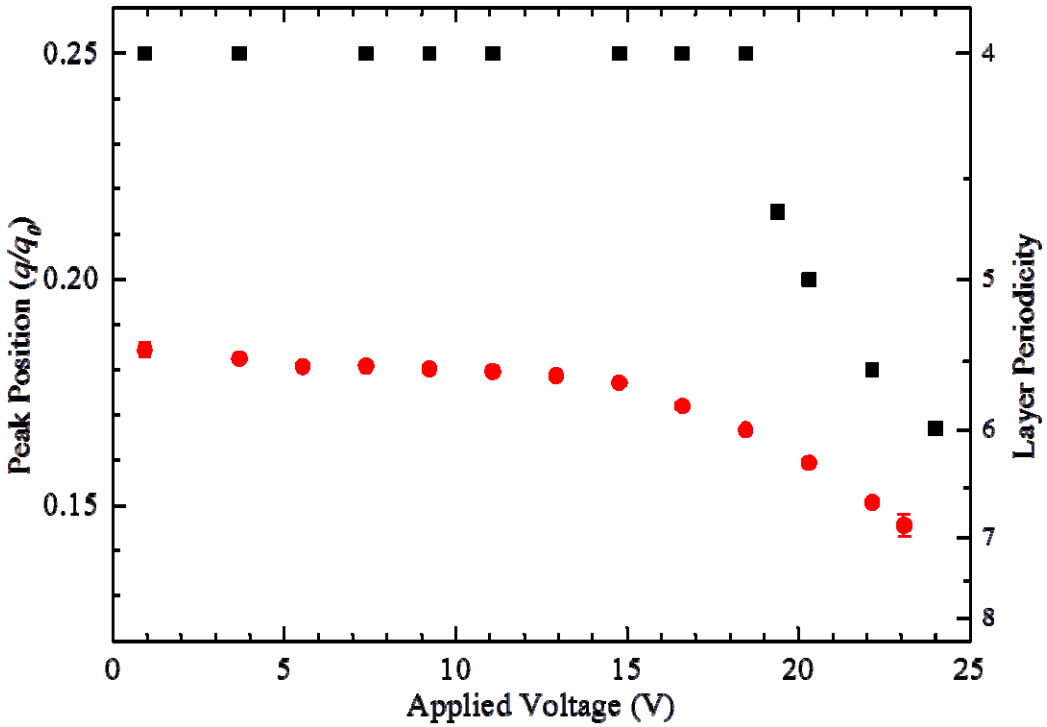
0.25
0.20
0.15
Peak Position (q/q_0)
4
5
6
7
8
Layer Periodicity
0
5
10
15
20
25
Applied Voltage (V)

Fig.9

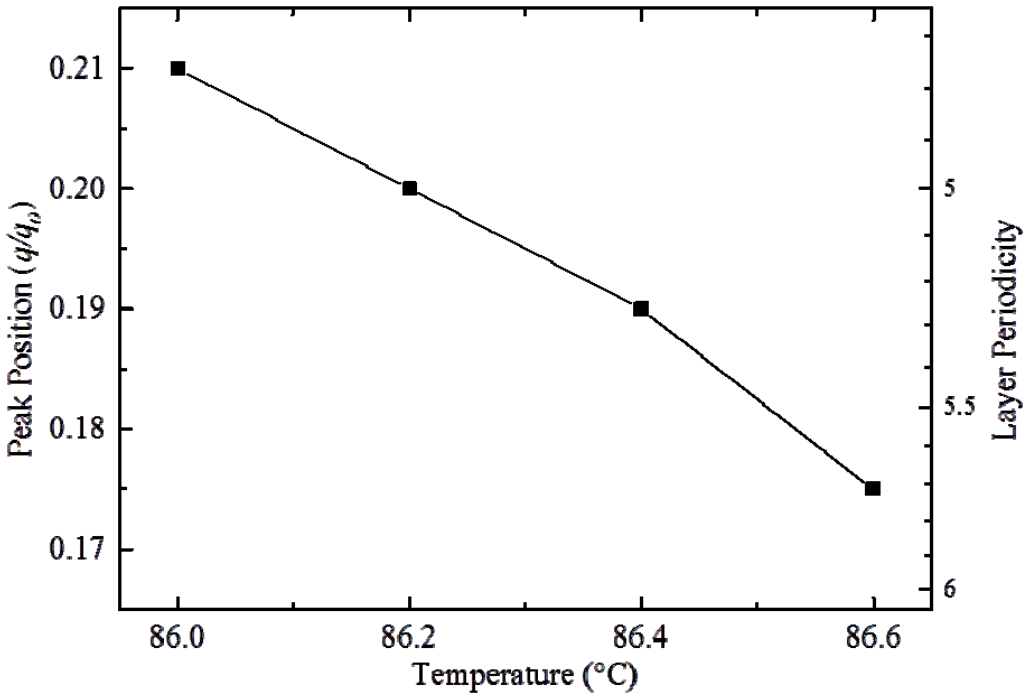
0.21
0.20
0.19
0.18
0.17
Peak Position (q/q_o)
5
5.5
6
Layer Periodicity
86.0
86.2
86.4
86.6
Temperature (°C)

Fig.10

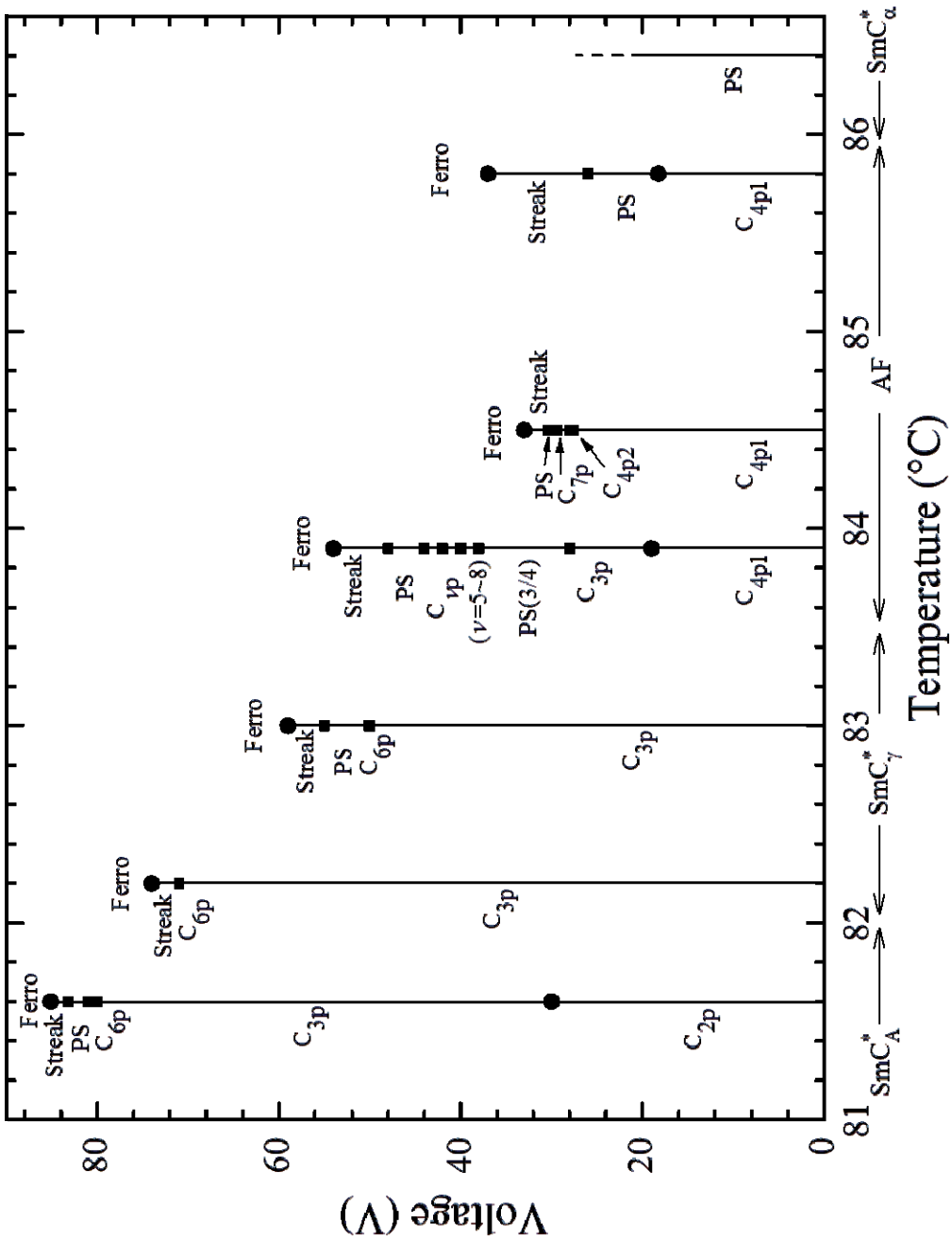
Voltage (V)
0
20
40
60
80
Temperature (°C)
81
82
83
84
85
86
SmC*A
SmC*γ
AF
SmC*α
Ferro
Streak
PS
C6p
C3p
C2p
C4p1
C4p2
C7p
Cνp
(ν=5~8)
PS(3/4)

Fig.11

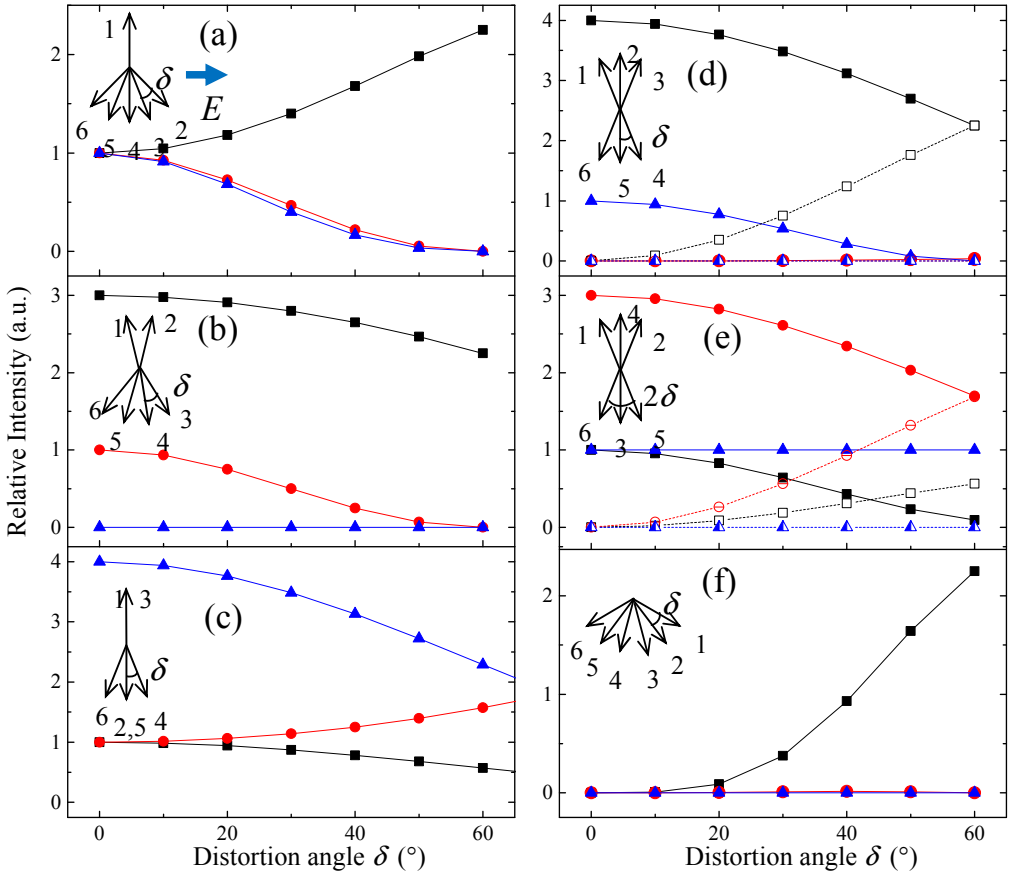
(a)
(b)
(c)
(d)
(e)
(f)
δ
E
2δ
Relative Intensity (a.u.)
Distortion angle δ (°)
Distortion angle δ (°)

Fig.12

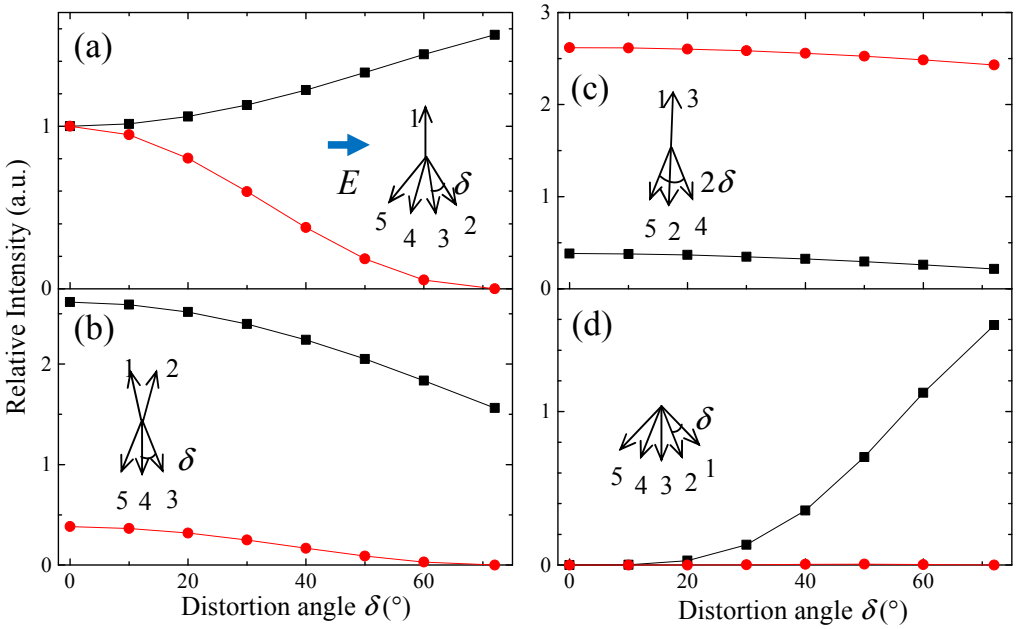
(a)
(b)
(c)
(d)
Relative Intensity (a.u.)
Distortion angle δ(°)
Distortion angle δ(°)
E
δ
2δ

Fig.13

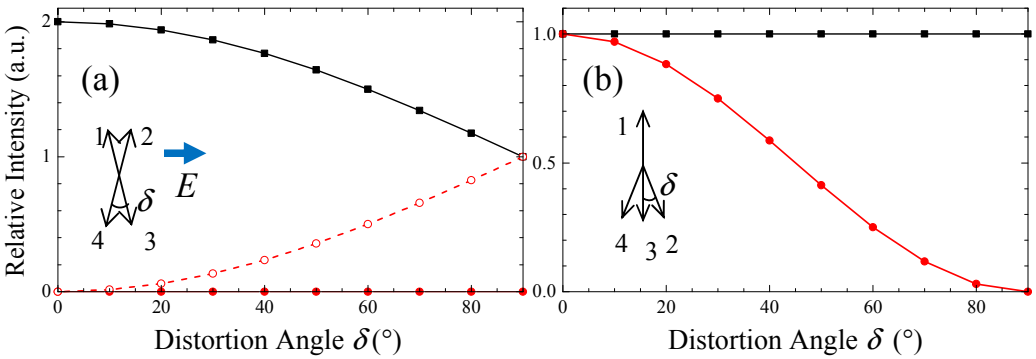
Relative Intensity (a.u.)
(a)
1
2
3
4
δ
E
Distortion Angle δ(°)
(b)
1
2
3
4
δ
Distortion Angle δ (°)

Fig.14